Explicit Risk Allocation for Cascaded Hydroelectric Systems Under Extreme Events

Eliza Cohn, *Student Member, IEEE*, Ning Qi, *Member, IEEE*, Upmanu Lall, and Bolun Xu, *Member, IEEE*

Abstract— Quantifying the impact of streamflow forecast uncertainty on short-term power generation in cascaded hydropower systems is critical for designing optimal operation strategies. Standard streamflow models determine the exogenous uncertainty, i.e. error occurring from environmental factors that are inputs into system, and is a form of *decision independent uncertainty* (DIU). In this paper, we propose a formulation based on endogenous uncertainty, which is achieved by conditioning the uncertainty in streamflow forecasts on release decisions from upstream units. This representation is a form of *decision dependent uncertainty* (DDU) and is incorporated when constructing the inflow forecasts into each hydropower unit. We formulate a system-wide optimization problem and use joint chance-constraints to constrain the random variables introduced from the inflow. We propose two different solution algorithms to demonstrate how our enhanced uncertainty representation increases system reliability and generates more energy. These results are verified under various network configurations and streamflow conditions. This work paves the way for the next generation of dynamic cascaded hydropower management.

Index Terms— Cascaded hydropower, decision-dependent uncertainty, joint chance-constraints, stochastic programming, short-term dispatch.

NOMENCLATURE

Functions
$\phi_i(\cdot)$ Hydraulic head function
Indices
i Index for hydro unit
j Index for upstream unit
t Index for time periods
Parameters
$1 - \varepsilon$ Reliability level
η_i Turbine efficiency
ρ Density of water ($1000 kg/m^3$)
c Conversion factor from J to MW ($3.6e^{-9}$)
g Gravitational acceleration ($9.8 m/s^2$)
n Number of hydro units
Sets
$\mathcal{I}$ Set of hydro units
$\mathcal{T}$ Set of time periods
Variables
$p_{i,t}$ Energy output (MWh)
$q_{i,t}$ Streamflow inflow rate (m^3/hr)
$s_{i,t}$ Reservoir spill outflow rate (m^3/hr)
$u_{i,t}$ Reservoir generation outflow rate (m^3/hr)
$v_{i,t}$ Reservoir volume (m^3)

I. INTRODUCTION

Ensuring reliable power supply from cascaded hydropower systems is challenging due to the spatiotemporal uncertainty that exists in networked streamflows. Existing inflow models across power systems and hydrology struggle to jointly capture seasonality, environmental drivers, and the influence of upstream release decisions within a unified analytical framework. Scheduling decisions for electricity generation occur over two stages. During the medium-term planning stage, the seasonal inflow forecast is calculated for the upcoming weeks. With this forecast, operators set target volume levels and allocate risk tolerance for the storage bounds. During short-term planning, the operators determine the hourly release schedule while considering short-term inflow forecast error. However, existing works assume that uncertainty in inflow is either absent or sufficiently characterized by a static forecast.

The paper proposes a real-time dispatch strategy that explicitly models forecast error such that the system to be robust under extreme weather events. To the best of our knowledge, no research work modeled DDUs of hydropower inflow models under a chance constrained optimization framework while proposing a computationally tractable solution that preserves the spatiotemporal relationship of the inflow forecast error. To fill in the research gap of both modeling and solution methodologies, this manuscript addresses the real-time joint chance-constrained optimization (CCO) problem of release dispatch for a cascaded hydropower network where both DIUs and DDUs can be considered. The main contributions of this manuscript are:

- i. *Modeling:* We propose a baseline cascaded hydropower model with a detailed uncertainty framework that can incorporates both DIUS and DDU. The DDU structure is learned from forecast residuals using a heteroskedastic variance model that conditions variance on prior variance, residual innovations, and upstream release decisions. This formulation allows the uncertainty representation to adapt dynamically to both system state, control actions, and extreme weather events by capturing the spatial propagation of forecast risk across the the cascade.
- ii. *Methodology:* Two tractable reformulations are developed to solve the CCO by decomposing the multi-period problem into a non-anticipatory framework that incorporates decision-dependent uncertainty. The Bonferroni approximation is used as a benchmark, decoupling system variance by assuming independence between units and reformulating individual chance constraints under a normal distribution. The supporting hyperplane algorithm is proposed to solve the original joint chance-constrained problem, leveraging the full covariance structure to enforce reliability requirements. We prove convergence of the supporting hyperplane algorithm and establish its convergence to the Bonferroni approximation under steady-state conditions.
- iii. *Numerical study:* We introduce a reliability metric, the *integrated violation index*, to assess the consequence of neglecting DDU during real-time dispatch. Using a two-step learning process, policies are trained under an inflow forecast model and

evaluated under historical inflow realizations. Across simulated dry-season droughts and wet-season floods, the DDU framework reduces constraint violations and maintains larger operational buffers against extreme events. This demonstrates how explicit risk allocation dynamically adjusts operations in response to evolving uncertainty and improves preparedness under both seasons.

II. LITERATURE REVIEW

Literature review on streamflow estimation, optimal cascaded hydropower operations, uncertainty representations in hydroelectric literature, chance constraints, and decision dependent uncertainty. Enumerate the contributions of this paper. [1] is a widely cited work that assumed upstream outflow can be modeled as downstream inflow with a constant time delay. This assumption ignores intermediary flow and localized hydrology processes, approximating the method presented in [2]. A widespread practice in hydrology literature to use an autoregressive process to model inflow dynamics while conditioning on various states derived from the environment. [3] introduces the DDUs and DIUs that this paper is modeled after. Authors in [4] present a 2D linear approximation for meshing the nonlinear power production function. Origins of supporting hyperplane for joint chance constraint programs by Prékopa and Szántai in [5] and [6]. We will also compare the standard forms of objective functions for hydropower operations to explain our motivation for maximizing generation and minimizing spill.

III. PROBLEM FORMULATION AND PRELIMINARIES

We consider a networked system of cascaded hydropower reservoirs consisting of n units $\mathcal{I} = \{1, 2, \ldots, n\}$ to be scheduled over the time horizon $\mathcal{T} = \{1, 2, \ldots, T\}$. Each unit is connected in series along the same river, and the matrix of streamflow observations into each unit is denoted by $Q \in \mathbb{R}^{T \times n}$. The streamflow inputs into the hydropower reservoirs $\hat{q}_t$ are modeled as a combination of the forecasted inflows μ_t predicted at the planning stage and the forecast deviations ξ_t revealed during real-time operations. We assume that ξ_t follows a distribution $\mathbb{P}$ centered around 0, following [7].

Fig. 1 gives a stylized illustration of why hydropower units operating along the same river give rise to inflow forecast errors that are spatially correlated. Because we explicitly model this process uncertainty in forecasting inflow, it is necessary to incorporate bilateral joint chance constraints that calculate the probability of maintaining reservoir volumes between both the upper and lower bounds for all units while preserving spatial correlation under the forecast uncertainty. This form of the joint chance-constraint was proposed by [8] and has become the standard for modeling multi-use reservoirs that incorporate both hydrologic and energy dispatch needs [9]. This energy dispatch problem gives rise to the following stochastic program:
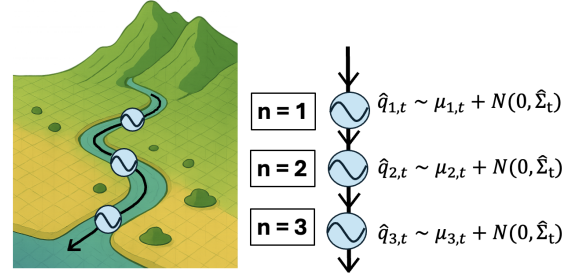

Fig. 1. Cascaded hydropower network with spatially correlated inflows

The objective function (1a) reflects the operators goal of maximizing power generation while minimizing spillage. Decision variable $p_t \in \mathbb{R}^n$ (MWh) denotes the dispatched energy for all hydropower units; $u_t \in \mathbb{R}^n$ (m³) denotes the water release intended for generation; $s_t \in \mathbb{R}^n$ (m³) denotes the remaining water release that becomes spill outflow; $v_t \in \mathbb{R}^n$ (m³) denotes the reservoir volume at end of each time period. All decisions are made at the hourly time step. The constraint (1b) tracks the volume state in the reservoirs based on the stochastic inflow $\hat{q}_t$ (m³), previous volume v_{t-1} (m³), and release decisions. The inflow forecast $\hat{q}_t \in \mathbb{R}^N$ is a linear combination of the deterministic mean forecast and the forecast uncertainty, and is characterized in III-B. The hydroelectric power production from water release is defined by (1c). A conversion from joule to MWh by parameter c (1MWh=$3.6e^9$Joule) ensures unit consistency on both sides of the constraint. (1d) models the water flow ramp rates $\underline{R}$ and $\overline{R}$, (1e) models the upper and lower water release bounds $\underline{U}$ and $\overline{U}$, and (1f) limits the total unit generation with the transmission capacity $\overline{P}$. (1g) constrains the upper bound on spillage, which is necessary in preventing uncontrolled spill during flood conditions [10]. The joint-chance constraint ensures volume bounds are satisfied with respect to inflow uncertainty is given in (1h), where ε represents the risk tolerance set by the operator. Applying chance constraints to the reservoir volume bounds is a critical step in encoding hydrologic uncertainty into a power system planning model.

Note that (1c) incorporates the nonlinear hydraulic head function that maps reservoir volume to effective water elevation. We assume that the relationship between volume and height is concave, following [11]. This exact form of the mapping from volume to head is typically fit from real-world data, and depends on the shape of the reservoir. This modeling framework follows the classical version of nonlinear cascaded hydropower optimization programs, which are stated in [1], [12], [13], and [14].

A. Convex Parameterization via Linear Reformulation

A piece-wise linear approximation is applied to the nonlinear power production function in (1c) to both convexify the constraint and increase tractability. The linear approximation uses a set of 1-D functions to partition the hydraulic head into N sub-intervals. The algorithm is

1) Calculate the N sub-intervals $I_i = [h_{i-1}, h_i)$ for $i = 1, 2, \ldots, N$ where $h_0 = h_{\min}$ and $h_N = h_{\max}$
2) Determine the optimal reference elevation $h_i^{\mathrm{ref}} = \arg\min_{h \in I_i} \mathbb{E}[\|g(h, u) - g(h_i^{\mathrm{ref}}, u)\|^2]$
3) Create the reference vector $H^{\mathrm{ref}} = [h_1^{\mathrm{ref}}, h_2^{\mathrm{ref}}, \ldots, h_N^{\mathrm{ref}}]$

This algorithm is well-suited to apply a convex parameterization over the bilinear term by calculating the hydraulic head reference from the previous volume term. During real-time scheduling, the algorithm is implemented as follows

1) Calculate the forebay elevation $h_t = \phi(v_{t-1})$

$$\max_{p,u,s,v} \quad \sum_{i \in \mathcal{I}} \sum_{t \in \mathcal{T}} (p_{i,t} - s_{i,t}) \tag{1a}$$

$$\text{s.t.} \quad v_{i,t} = v_{i,t-1} + \hat{q}_{i,t} - (u_{i,t} + s_{i,t}) \tag{1b}$$

$$p_{i,t} = c\,\eta g \rho\, \phi(v_{i,t})\, u_{i,t} \tag{1c}$$

$$\underline{R} \leq u_{i,t} - u_{i,t-1} \leq \overline{R} \tag{1d}$$

$$\underline{U} \leq u_{i,t} \leq \overline{U} \tag{1e}$$

$$0 \leq p_{i,t} \leq \overline{P} \tag{1f}$$

$$0 \leq s_{i,t} \leq \overline{S} \tag{1g}$$

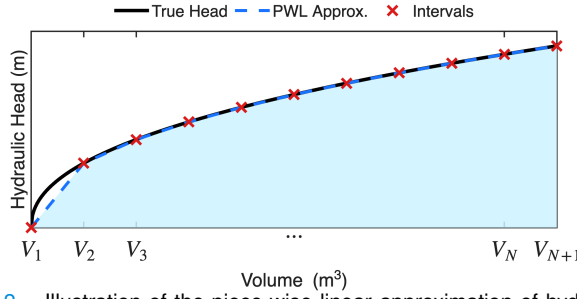$$\mathbb{P}[\underline{V} \leq v_{i,t} \leq \overline{V}] \geq 1 - \varepsilon \tag{1h}$$

Fig. 2. Illustration of the piece-wise linear approximation of hydraulic head function over a normalized volume range with 10 sub-intervals.

2) Find sub-interval index $i^* = \arg\max_i\{h_t \in I_i\}$ and retrieve the reference elevation $h^{\text{ref}} = h_{i^*}^{\text{ref}}$
3) Approximate the power production function
$p_t \approx c\eta g\rho h^{\text{ref}} u_t$

We visualize the piece-wise linear approximation of the hydraulic head function in Fig. 2.

The volume has been normalized to enable comparison between units with different storage capacities while preserving the nonlinear relationship between storage and head. We note that this function defines why generation efficiency is reduced at low storage levels. Indexing the reference hydraulic head with the previous volume state decomposes the multi-period framework into a non-anticipatory framework that is solved sequentially for each time step, taking advantage of the nature of the two-stage scheduling process, since real-time decisions are finalized once the inflow forecast uncertainty is observed.

B. Inflow and Uncertainty Characterization

Real-time dispatch of hydroelectric operations relies on inflow forecasts that are inherently uncertain. We model inflow as a Gaussian random variable whose mean equals the deterministic forecast and variance representing forecast uncertainty, which may vary over time [15]. Although inflow is nonnegative, we do not adopt a log-normal specification, as the Gaussian assumption preserves analytical tractability of the resulting chance-constrained formulation. For each time step, we define the inflow distribution as

$$\hat{q}_t = \mu_t + \xi_t, \quad \xi_t \sim \mathcal{N}(0, \hat{\Sigma}_t) \tag{2}$$

where $\hat{q}_t$ is the vector of random inflow realizations, μ_t denotes the deterministic inflow forecasts, and ξ_t represents the stochastic forecast error with spatial covariance Σ_t. The forecast for each unit is obtained via a linear regression model of the form

$$\mu_{i,t} = \alpha_0 + \sum_{n=1}^{p} \alpha_n q_{i,t-n} + \sum_{m=1}^{q} \beta_m(u_{j,t-m} + s_{j,t-m}) \tag{3}$$

where $q_{i,t-n}$ are previous observed inflow terms and $(u_{j,t-m} + s_{j,t-m})$ are previous water releases from the upstream unit. By including the local flow and system dynamics in the inflow forecast, we can capture both the effects of the surrounding ecosystem and the release decisions made by upstream units.

Let $\hat{q}_{i,t}$ denote the inflow forecast obtained from the regression model in (3), and let $q_{i,t}$ denote the observed inflow realization. The forecast residual is defined as

$$e_{i,t} = q_{i,t} - \hat{q}_{i,t}, \tag{4}$$

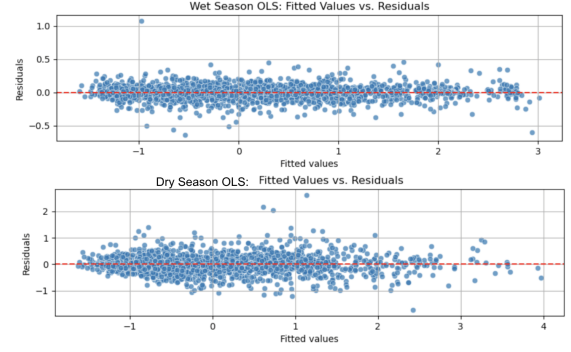where we collect these into the residual vector $e_t = (e_{1,t}, \ldots, e_{n,t})^T$.

Fig. 3. Nonstationary variance of inflow forecast residuals

Reservoir operators typically estimate the deviation from inflow forecasts under a decision-independent framework, calculating static uncertainty sets from historical data. However, this can lead to aggressive control policies, leaving little buffer room for handling extreme events. Decision-dependent uncertainty representations incorporates upstream release decisions into the estimation framework, quantifying how the release strategies of upstream units impacts the covariance matrix for the normal distribution. We show that this enhanced modeling sensitivity can lead to more conservative variance estimates.

1) Decision-Independent Uncertainty: Under DIU, the covariance matrix is static and estimated offline from the residuals of historical streamflow forecasts. Let $e_t = (e_{1,t}, ..., e_{n,t})^T$ denote the vector of forecast residuals. We then estimate the DIU forecast-error covariance matrix as

$$\hat{\Sigma}^{DIU} = \frac{1}{T-1} \sum_{t=1}^{T} (e_t - \bar{e})(e_t - \bar{e})^T \tag{5a}$$

$$\hat{\sigma}^{DIU} = \sqrt{\text{diag}\left(\hat{\Sigma}^{\text{DIU}}\right)} \tag{5b}$$

The per-unit variance terms in (5b) are constant under the assumption of DIU. Because the covariance matrix is fixed over time, it is independent of operational decisions. Estimating the spatial variance from regression residuals captures the cross-unit forecast uncertainty not explained by the deterministic inflow model [16].

2) Decision-Dependent Uncertainty: Under DIU, the covariance matrix is assumed constant over time and independent of system operations. However, empirical analysis of the forecast residuals reveals non-stationarity with respect to upstream release decisions, as shown in Fig. 3. This heteroskedastic behavior violates the stationarity assumption of DIU and can lead to poorly calibrated reliability guarantees. Fig. 4 summarizes the learning algorithm that synthesizes offline parameter estimation with real-time state updates create the dynamic DDU covariance matrix given below:

$$\hat{\Sigma}_t^{DDU} = \begin{pmatrix} (\hat{\sigma}_{1,t}^{DDU})^2 & \cdots & \hat{\rho}_{1n}\hat{\sigma}_{1,t}^{DDU}\hat{\sigma}_{n,t}^{DDU} \\ \vdots & \ddots & \vdots \\ \hat{\rho}_{n1}\hat{\sigma}_{n,t}^{DDU}\hat{\sigma}_{1,t}^{DDU} & \cdots & (\hat{\sigma}_{n,t}^{DDU})^2 \end{pmatrix} \tag{6a}$$

$$\hat{\sigma}_{i,t}^{DDU} = \sqrt{\omega + \xi e_{i,t-1}^2 + \zeta\sigma_{t-1}^2 + \gamma(u_{j,t-1} + s_{j,t-1})} \tag{6b}$$

Let $\rho_{i,j}$ refer to the correlation coefficient between the forecast residuals of units i and j. To model the time-varying volatility structure and capture the spatial correlation of inflows, we employ the generalized autoregressive conditional heteroskedasticity (GARCH) model proposed by Bollerslev in [17] to estimate the heteroskedastic variance as a linear combination of past squared residuals and past
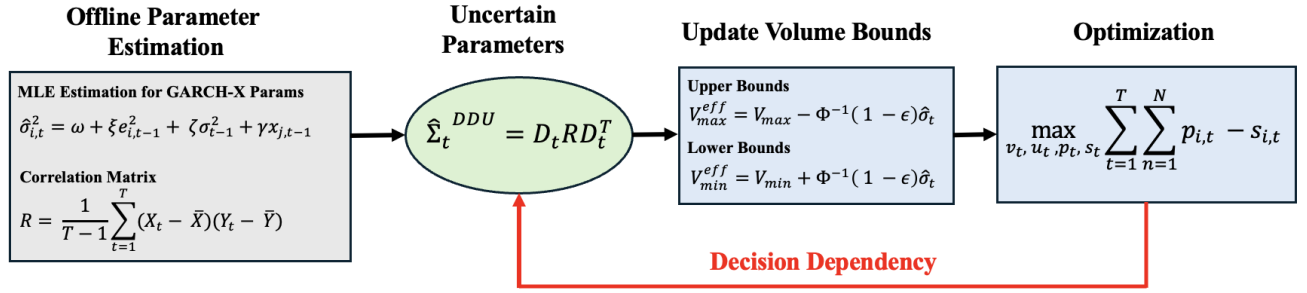
Fig. 4. Block diagram of online and state-dependent variance estimation

squared variance. We extend this model to incorporate the total upstream release as an additional exogenous predictor to complete the full characterization of (6b). The parameters $(\omega, \xi, \zeta, \gamma)$ are estimated using maximum likelihood [18]. We use the index j to refer to the upstream unit. This estimation captures how forecast uncertainty evolves in response to both intrinsic inflow variability and upstream operational decisions. The parameter ω represents the baseline variance level, ξ captures the impact of recent forecast errors, and ζ models volatility persistence over time. The coefficient γ quantifies the influence of upstream release and spill decisions on downstream forecast uncertainty, reflecting the physical propagation of flow variability through the cascade.

IV. SOLUTION METHODOLOGY

Two approaches are proposed to solve the joint chance-constrained optimization problem in (1). add papers to cite why this is np-hard to solve, and give solution approaches The Bonferroni approximation decomposes the joint chance constraint into individual constraints using preset risk allocations, yielding a tractable but conservative reformulation based on marginal variance estimates. In contrast, the supporting hyperplane algorithm enforces the joint chance constraint directly by incorporating the full covariance structure of inflow uncertainty. This distinction is particularly important under decision-dependent uncertainty, where dynamic covariance coupling cannot be fully captured by marginal approximations.

A. Bonferroni Solution Algorithm

The Bonferroni approximation solves the joint chance constraint in (1h) by assuming spatial independence and decomposing the single chance constraint into a set of individual chance constraints whose combined violation probability is bounded through the union bound. The orginal joint chance constraint is

$$\mathbb{P}\left(\bigcap_{i=1}^{n} \underline{V}_i \leq v_{i,t} \leq \overline{V}_i\right) \geq 1 - \varepsilon, \tag{7}$$

After selecting the risk tolerance ε, each constraint i is allocated an equal violation budget ε_i such that

$$\varepsilon_i^{BON} = \frac{\varepsilon}{n}, \qquad \sum_{i=1}^{m} \varepsilon_i = \varepsilon \tag{8}$$

By assuming a Gaussian form for the inflow forecasts, the individual chance constraints are reformulated into deterministic constraints by adding a safety margin that is the product of the standard normal quantile $z = \Phi^{-1}(1 - \varepsilon_i^{BON})$ and the standard deviation term. The deterministic volume bounds for unit i are given as

$$\underline{V}_i^{eff} = \underline{V}_i + z\hat{\sigma}_i \tag{9a}$$
$$\overline{V}_i^{eff} = \overline{V}_i - z\hat{\sigma}_i \tag{9b}$$

Combining the substitution of the mean inflow forecast into (1b) and the safety bounds proposed in (9) completes the solution algorithm under the Bonferroni approximation. We note that standard deviation estimated under both DIU and DDU are suitable for incorporating into the volume bounds. A key characteristics of the Bonferroni approximation is that it cannot adaptively relax or tighten its bounds. This makes it a simple and convex solution suitable for standard operating conditions and moderate drought or flood events.

B. Supporting Hyperplane Solution Algorithm

We present the matrix representation of the linearized and convex optimization problem.

$$\min_{x_t \in \mathbb{R}^n, x \geq 0} c^T x_t \tag{10a}$$

$$\text{s.t.} \quad A_t x_t \leq b_t \tag{10b}$$
$$v_t = v_{t-1} + \hat{q}_t - (u_t + s_t) \tag{10c}$$
$$\mathbb{P}[\underline{V} \leq v_t \leq \overline{V}] \geq 1 - \varepsilon \tag{10d}$$

where we define the per-timestep portion of each matrix as

$$A_t = \begin{pmatrix} 1 & -c\eta g\rho h_t^{ref} & 0 & 0 \\ 0 & 1 & 0 & 0 \\ 0 & -1 & 0 & 0 \\ 0 & 1 & 0 & 0 \\ 0 & -1 & 0 & 0 \\ 1 & 0 & 0 & 0 \end{pmatrix} \quad b_t = \begin{pmatrix} 0 \\ \overline{U} \\ -\underline{U} \\ \overline{R} + u_{t-1} \\ \underline{R} - u_{t-1} \\ \overline{P} \end{pmatrix}$$

$$x_t = \begin{pmatrix} p_t \\ u_t \\ s_t \\ v_t \end{pmatrix} \quad c_t = \begin{pmatrix} -1 \\ 0 \\ 1 \\ 0 \end{pmatrix}$$

The supporting hyperplane algorithm maintains spatial correlation between units and solves the joint chance constraint directly, requiring the cumulative distribution function (CDF) for the multivariate gaussian distribution that characterizes the inflow in the region. Evaluating the CDF over all the hydropower units allows us to identify which unit is the most at risk for violating volume boundaries. The general form of a CDF for $X \sim \mathcal{N}(\mu, \Sigma)$ at a points $a, b \in \mathbb{R}^n$ with $a_i \leq b_i$ is

$$F_X(a,b) = \mathbb{P}(a \leq X \leq b) = \int_{a_1}^{b_1} \cdots \int_{a_n}^{b_n} f_X(t)dt \quad (11)$$

where $f_X(t)$ is the corresponding probability density function. We reformulate (7) to surround the random inflow variable $\hat{q}$ by substituting the mass balance equation for v_t and recomputing the bounds.

$$\mathbb{P}[\underline{V}' \leq \hat{q}_t \leq \overline{V}'] \geq 1 - \varepsilon \quad (12a)$$
$$\underline{V}' = \underline{V} - v_{t-1} + (u_t + s_t) \quad (12b)$$
$$\overline{V}' = \overline{V} - v_{t-1} + (u_t + s_t) \quad (12c)$$

Combining (11) and (12) derives an explicit formulation for evaluating the probability of volume bound violations given the current state.

$$F(\underline{V}', \overline{V}') = \frac{1}{(2\pi)^{n/2}|\hat{\Sigma}_t|^{1/2}} \int_{\underline{V}'_1}^{\overline{V}'_1} \cdots \int_{\underline{V}'_n}^{\overline{V}'_n} e^{-\frac{1}{2}(x-\mu)^\top \hat{\Sigma}_t^{-1}(x-\mu)} dx \quad (13)$$

The CDF presented in (13) and its gradient can be numerically evaluated following the code in [19] and [20]. In practice, the finite difference method is sufficient for evaluating the gradient. The algorithm proposed in (1) is an extension of the methods from [8]. We adapt the algorithm to be solved sequentially and incorporate the real-time updates of the covariance matrix based in upstream release decisions.

Algorithm 1: Sequential Supporting Hyperplanes

Input : Solution x_t^{LP} to (10), a point x_t^s that is feasible for (10) and satisfies (12), and $\hat{\Sigma}_t$
Output: Solution x^* to (1)
for $t = 1$ **to** T **do**
  Initialization: $k = 0$, $(x_t^0, A_t^0, b_t^0) \leftarrow (x_t^{LP}, A_t, b_t)$
  while $\|x_t^{k+1} - x_t^k\|_\infty > tol$ **do**
    Step 1: Interpolation
    Find $\lambda^* \in (0,1)$ such that $x_t^{k*} = (1-\lambda^*)x_t^k + \lambda^* x_t^s$
    and
    $F[\underline{V}'(x_t^{k*}), \overline{V}'(x_t^{k*})] \geq 1 - \varepsilon$
    Step 2: Add Cut
    Add the hyperplane to the system
    $\nabla F_k^T(x_t - x_t^{k*}) \leq 0$
    $A_t^{k+1} \leftarrow A_t^k \cup \{\nabla F_k^T\}$ $b_t^{k+1} \leftarrow b_t^k \cup \{\nabla F_k^T x_t^{k*}\}$
    Step 3: Solve the updated LP
    Solve the updated linear program:
    $$x_t^{k+1} = \arg\min\{c^T x_t \mid A_t^{k+1} x_t \leq b_t^{k+1}, x_t \geq 0\}$$
    if $\|x_t^{k+1} - x_t^k\|_\infty < tol$ **then**
    | **break**
    end
    $k \leftarrow k + 1$
  end
  Store $x_t^* \leftarrow x_t^k$
  Update $\hat{\Sigma}_{t+1}$
end
return x_t^*

The proof of convergence for the supporting hyperplane algorithm is given in constructs a polyhedral approximation of the feasible region through hyperplane cuts that tightens the bounds on risky units while loosening the bounds on the safer units. We prove that the sequential supporting hyperplane algorithm either converges to

the optimal solution in a finite number of iterations or generates a sequence of solutions which converges to a global optimum, and defer the complete proof to Appendix 2. This proof follows the structure of the convergence proof in [21]. We note that by construction, $\hat{\Sigma}_t^{DDU}$ is guaranteed to be positive definite and can be computing efficiently via the Cholesky decomposition.

A Slater point x_t^s is necessary for the initializing the interpolation in Step 2. To equations used to determine x_t^s are given in (14), where we determine a feasible starting point by proposing a conservative release policy and calculating the next state. This ensures that x_t^s is feasible and will not violate volume bounds. The Slater point initialization algorithm is

$$u_t^s = \max\{\underline{U}, u_{t-1} - \underline{R}\} \quad (14a)$$
$$s_t^s = \max\{0, v_{t-1} + \hat{q}_t - u_t^s\} \quad (14b)$$
$$v_t^s = v_{t-1} + \hat{q}_t - (u_t^s + s_t^s) \quad (14c)$$
$$p_t^s = c\eta g\rho\phi_i(v_t^s)u_t^s \quad (14d)$$

where the release policy proposed in (14a) is the most conservative release policy available, either proposing full curtailment or maintaining the minimum release level. The spill is calculated in (14b) by determining if any overflow will occur after the release policy is decided. The volume state and power generation is calculated in (14c) and (14d).

what's the main extension for this algorithm? maybe we don't need to say that way? The key of SSH is to ensure distribution is concave, and constraints are convex? So we can not use binaries here. Write about supporting hyperplane under DDU

C. Risk Attribution Signal

The following theorem derives a closed-form representation of the risk attribution signal derived from the supporting hyperplane algorithm. We make the following assumptions on the underlying streamflow distribution and cumulative distribution function (13).

Assumption 1: The inflow random variable $\hat{q}_t \in \mathbb{R}^n$ follows a multivariate Gaussian distribution $\hat{q}_t \sim \mathcal{N}(\mu_t, \Sigma_t)$ with $\Sigma_t \succ 0$.

Remark 1: Alternate distributions, such as the log-normal, can also be assumed in this framework. In that case, chance constraints would be evaluated using Monte Carlo sampling or moment-based bounds derived from the mean and covariance.

Property 1: The joint chance constraint on reservoir volumes can be written as a rectangular probability over the inflow variable and we define the CDF as

$$F_t := \mathbb{P}(\underline{V}'_t \leq \hat{q}_t \leq \overline{V}'_t) \quad (15)$$

where the bounds are defined in (13). Therefore, the mapping from (v_{t-1}, s_t, u_t) to $(\underline{V}'_t, \overline{V}'_t)$ is continuously differentiable.

Property 2: $F(\underline{V}'_t, \overline{V}'_t)$ is log-concave, monotonically non-decreasing, right-continuous, and differentiable when $\Sigma_t \succ 0$.

Proposition 1: Let the system reliability with respect to volume bounds be defined in (15). We define gradient of the system reliability with respect to the volume state as

$$\frac{\partial F_t}{\partial v_{i,t-1}} = -\frac{\partial F_t}{\partial \underline{V}'_{i,t}} - \frac{\partial F_t}{\partial \overline{V}'_{i,t}} \quad (16)$$

The expression relates how the contribution of the volume state to system reliability for each hydropower unit is proportional the effective inflow bounds, motivating the introduction of the "risk attribution signal", defined as

$$\alpha_{i,t} = \frac{\left|\frac{\partial F_t}{\partial v_{i,t-1}}\right|}{\sum_{j=1}^{n}\left|\frac{\partial F_t}{\partial v_{j,t-1}}\right|} \tag{17}$$

Where $\alpha_{i,t}$ is a measure of how strongly each unit contributes to the overall probability system remains in the safe operating region. Specifically, $\alpha_{i,t}$ represents the relative marginal contribution of unit i's state to first-order changes in system risk, which we define as $R_t := 1 - F_t$.

Proof: Since $\Sigma_t \succ 0$, the multivariate Gaussian density is smooth and the rectangle probability F_t is differentiable with respect to its bounds V'_t and $\overline{V}'_t$.

Applying the chain rule gives

$$\frac{\partial F_t}{\partial v_{i,t-1}} = \sum_{k=1}^{n}\left(\frac{\partial F_t}{\partial V'_{k,t}}\frac{\partial V'_{k,t}}{\partial v_{i,t-1}} + \frac{\partial F_t}{\partial \overline{V}'_{k,t}}\frac{\partial \overline{V}'_{k,t}}{\partial v_{i,t-1}}\right).$$

From the definitions of V'_t and $\overline{V}'_t$,

$$\frac{\partial V'_{k,t}}{\partial v_{i,t-1}} = \frac{\partial \overline{V}'_{k,t}}{\partial v_{i,t-1}} = -\mathbf{1}\{k = i\},$$

which yields

$$\frac{\partial F_t}{\partial v_{i,t-1}} = -\frac{\partial F_t}{\partial V'_{i,t}} - \frac{\partial F_t}{\partial \overline{V}'_{i,t}}.$$

Thus (16) represents the marginal effect of unit i on system risk, and normalization yields the attribution signal $\alpha_{i,t}$.

Corollary 1: Under the conditions of Proposition 1, if the risk attribution weights are strictly positive, then the weights are normalized

$$\alpha_{i,t} \in [0,1], \qquad \sum_{i=1}^{n}\alpha_{i,t} = 1.$$

Theorem 1: If the inflow distribution and state-to-bound mappings are symmetric across units, then

$$\left|\frac{\partial F_t}{\partial v_{1,t-1}}\right| = \cdots = \left|\frac{\partial F_t}{\partial v_{n,t-1}}\right|,$$

and

$$\alpha_{i,t} = \frac{1}{n}, \quad \forall i.$$

Proof:

This theorem is equivalent to showing that under the steady-state conditions $\Delta x_t \to 0$, the risk attribution weights become equal across all units, such that

$$\alpha_{1,t} = \cdots = \alpha_{n,t}$$

Because the denominators for $\alpha_{i,t}$ are identical for $\forall i$, this is equivalent to showing

$$\left|\frac{\partial F_t}{\partial v_{1,t-1}}\right| = \cdots = \left|\frac{\partial F_t}{\partial v_{n,t-1}}\right|$$

Plugging in our definition we derived in Proposition 1 and evaluating the absolute values, we rewrite this as

$$\frac{\partial F_t}{\partial \underline{V}'_{1,t}} + \frac{\partial F_t}{\partial \overline{V}'_{1,t}} = \cdots = \frac{\partial F_t}{\partial \underline{V}'_{n,t}} + \frac{\partial F_t}{\partial \overline{V}'_{n,t}}$$

We begin by showing the upper bound gradients are equal across all units during steady state. To do this, we state the define the gradient of (11) with respect to boundary conditions [20] as

$$\frac{\partial}{\partial b_i}F_\xi(a,b) = f_{\xi_i}(b_i)F_{\tilde{\xi}(b_i)}(\tilde{a},\tilde{b}) \tag{18a}$$

$$\frac{\partial}{\partial a_i}F_\xi(a,b) = -f_{\xi_i}(a_i)F_{\tilde{\xi}(a_i)}(\tilde{a},\tilde{b}) \tag{18b}$$

where f_{ξ_i} is the corresponding probability density function, and $F_{\tilde{\xi}(a_i)}(\tilde{a},\tilde{b})$ denotes the two-side cumulative distribution function with the contribution from component a_i removed. It is defined symmetrically for b_i as well.

From (16), we know that the risk attribution weights are defined by the linear combination of volume bounded gradients. Using (12), we note that $\underline{V}'$ and $\overline{V}'$ are functions of the control policies, which we can write explicitly as $\underline{V}'(x_t)$ and $\overline{V}'(x_t)$. Plugging in our definitions to the general form of (18), we want to show that when $\Delta x_t \to 0$

$$\frac{\partial}{\partial \overline{V}'_1(x_t)}F_\xi(\underline{V}',\overline{V}') = \cdots = \frac{\partial}{\partial \overline{V}'_n(x_t)}F_\xi(\underline{V}',\overline{V}')$$

The rest of this proof is deferred to the appendix.

Lemma 1: Under the state-state conditions of Theorem 1, we see that the risk attribution weights in (17) converge to the Bonferroni bounds in (8).

$$\varepsilon_i^{SSH} \to \frac{\varepsilon}{n} \tag{19a}$$

$$\varepsilon_i^{SSH} = \varepsilon\alpha_{i,t} \tag{19b}$$

V. CASE STUDIES

In this section, case studies are conducted in MATLAB with a laptop with a Apple M3 4.1 GHz CPU and 16 GB of RAM. Gurobi 12.02 is used as the solver.

A. Setup

We consider a cascaded hydropower system consisting of three units in series. For the real time scheduling of the hydro units, 84 hourly periods are considered, i.e. $\tau = \{1,...,84\}$. 40 segments are used for the piece-wise linear approximation of the power production function. Each unit is identical in volume, generating capacity, and ramp rate capabilities. The generating capacity of each unit is 1 MW with a 90% generating efficiency. The volumetric and flow parameters have been normalized to the per-unit scale, such that the volume of each unit is designed to map $v_t \in [0,1]$ and $u_t \in [0.01, 0.05]$. The hydraulic head coefficients a and b are 5 and 0.45, mapping a full reservoir volume to the max effective voltage of 5V. The ramp rates are 0.01 and 0.015 for ramp-up and ramp-down capabilities respectively. The risk tolerance for violating volume bounds is set to $\varepsilon = 0.05$. I think we need to clarify all the units here.

1) Mean Forecast: It is estimated that the standard travel time between hydro units is $\tau^* = 3$, and recall that j is the index of the upstream unit. The mean inflow forecast is initially held constant between uncertainty frameworks for preliminary benchmarking. The set of parameters used in the mean inflow forecast are $(\alpha_0, \alpha_1, \beta_1, p, q) = (0.002, 0.95, 0, 1, 1)$.

2) DIU Characterization: The static covariance matrix used for the DIU representation of uncertainty is computed following (5). For the Bonferroni approximation, we assume spatial independence calculate the per-unit standard deviations by taking the square root of its diagonal elements. consider other ways of showcasing parameter results, especially how params vary by season
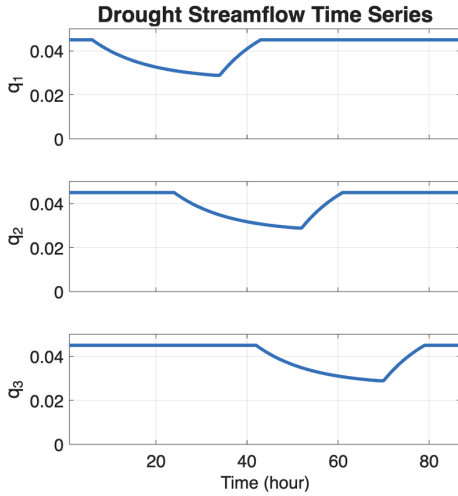
Fig. 5. Time-flow series representing drought scenarios propagating down three cascaded hydropower units in series.

3) DDU Characterization: The static correlation matrix used in the DDU representation of uncertainty is computed following (**??**). The parameters used in the dynamic GARCH-X estimations of the per-unit standard deviations from (6b) were derived via MLE and normalized. We note that $\zeta = 0$, indicating the memory-less property of GARCH-X estimations when applied to streamflow data.

B. Drought Scenarios

During the dry season, hydropower operators face the challenge of maintaining both generation and minimum flow requirements while inflow is low and demand is high. Unexpected droughts can severely strain the system, requiring robust reliability measures to ensure the hydropower unit can maintain operations if inflow becomes unexpectedly constrained. We represent this by initializing all units to start with the initial volume condition of 10% capacity.

Step 1: Learning Dry Season Optimal Trajectories
We present a drought scenario in Fig. 5 under the following settings. Consider an initial estimation of the nominal streamflow to be $q_0 = 0.045$, which is 10% below the maximum water release bound. The drought event is modeled as an exponential decay over 28 hours with a minimum amplitude scaled to be -40% of the nominal flow. The first 18 hours of the drought are the decay and the final 10 hours are a linear restoration to the nominal flow. Each hydropower unit experiences one drought event, and the drought propagates between units over 18 hours. Let the deterministic uncertainty framework be abbreviated by DET and have it refer to the baseline scenarios where inflow variance is set to zero for all units.

Fig. 6 compares the optimal policy trajectories for the cascaded hydropower units under drought conditions across uncertainty formulations (DET, DIU, DDU) and solution methods (Bonferroni, SSH). Because the framework assumes the demand for electricity is larger than the generation capacity, all units are incentivized to ramp up water release to maximum flow rates until their storage is depleted. The parameters in the GARCH-X variance model were trained on historical data and indicate that DDU estimations of variance are up to 50% larger than the DIU estimates. This leads to conservative chance-constrained volume bounds and a tighter feasible region. DDU alters the policy by curtailing releases earlier during the drought. Once the event subsides, all policies converge to the same steady-state release level but with DDU resting at a higher hydraulic head due to its earlier conservation.

Table I summarizes the system performance under solution algorithms and uncertainty frameworks. It confirms the intuition that

TABLE I
BENCHMARKING ENERGY GENERATION AND EFFICIENCY UNDER DROUGHT SCENARIOS

Algorithm	Metric	DET	DIU	DDU
Bonferroni	System Total Energy [MWh]	9.92	13.53	14.76
	Unit 1	2.24	3.81	3.81
	Unit 2	3.48	4.66	5.37
	Unit 3	4.20	5.05	5.57
	System Efficiency [MWh/m^3]	0.93	1.27	1.39
SSH	System Total Energy [MWh]	9.92	13.48	14.89
	Unit 1	2.24	3.77	4.00
	Unit 2	3.48	4.66	5.34
	Unit 3	4.20	5.05	5.56
	System Efficiency [MWh/m^3]	0.93	1.27	1.41

the larger safety buffers under DDU leads to a higher generation efficiency, a direct result of the nonlinear power production function increasing generation efficiency at higher forebay elevations. Therefore, DDU provides a mechanism for valuing storage under a single-period dispatch structure. SSH demonstrates a small improvement in the system's total generation capacity compared to Bonferroni, but we note that the algorithms largely converge in performance due to physical constraints (available water, flow limits, ramp rates) governing system behavior under drought conditions.

Fig. 7 showcases a unique feature of the SSH algorithm is its ability to calculate the latent risk state. This effective risk budget is a byproduct of evaluating the joint probability distribution directly while making the hyperplane cuts, as seen in (17). We leverage this term to trace how the risk propagates through the cascaded hydropower units. Under decision-independent uncertainty, risk is shared equally across units when they enter the low-volume operating conditions induced by the drought scenario. Under decision-dependent uncertainty, risk allocation still propagates but now asymmetrically because the upstream unit stabilizes its release policy after the drought has passed and its share of risk becomes absorbed by the downstream units. This adaptive redistribution of risk illustrates how SSH highlights the units most exposed to constraint violations.

Step 2: Monte Carlo Simulations under Drought Events
Monte Carlo simulations are performed to test how the optimal policy trajectories perform under uncertainty realizations. The experiment has the following procedures:

1) Select K = 500 Monte Carlo samples of real-time realizations of inflow realizations under decision-dependent uncertainty.
2) Perform real-time dispatch of the cascaded hydropower system under drought conditions.
3) Record the average system constraint violations.

To quantify how the system performs under Monte Carlo simulations, we define the following metric. The expected magnitude of the constraint violation is calculated by the integration violation index (IVI), and quantifies the severity of the volume constraint violation. It is defined as:

$$\text{IVI} = \mathbb{E}\big[\max(\underline{V} - v, 0) + \max(v - \overline{V}, 0)\big] \quad (20a)$$

$$\text{IVI} = \frac{1}{TN} \sum_{i=1}^{N} \sum_{t=1}^{T} \max(\underline{V}_i - v_{i,t}, 0) + \max(v_{i,t} - \overline{V}_i, 0) \quad (20b)$$

Table II shows that across both solution algorithms, reliability improves as the uncertainty model becomes more informative. Under Bonferroni, transitioning from DET to DIU and then DDU reduces the Integrated Violation Index (IVI) from 2.14 to 1.79 and 1.51, respectively, indicating progressively fewer and less severe violations
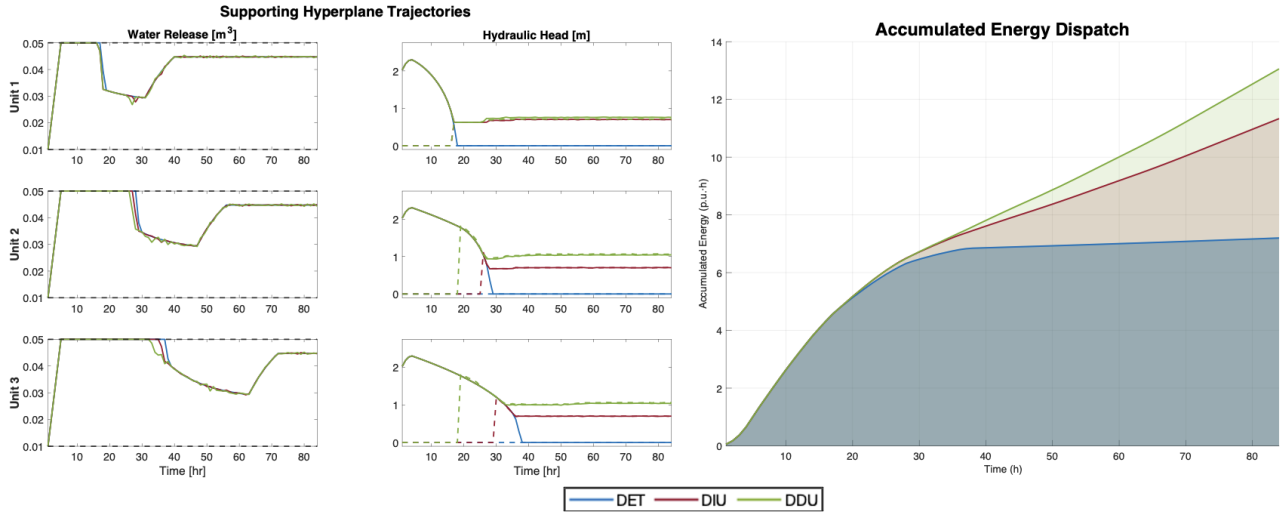
Fig. 6.   Optimal policy trajectories for water release, reservoir volume, and energy generation under DET, DIU, and DDU uncertainty frameworks using the supporting hyperplane solution algorithm. Dashed lines indicate operating bounds.
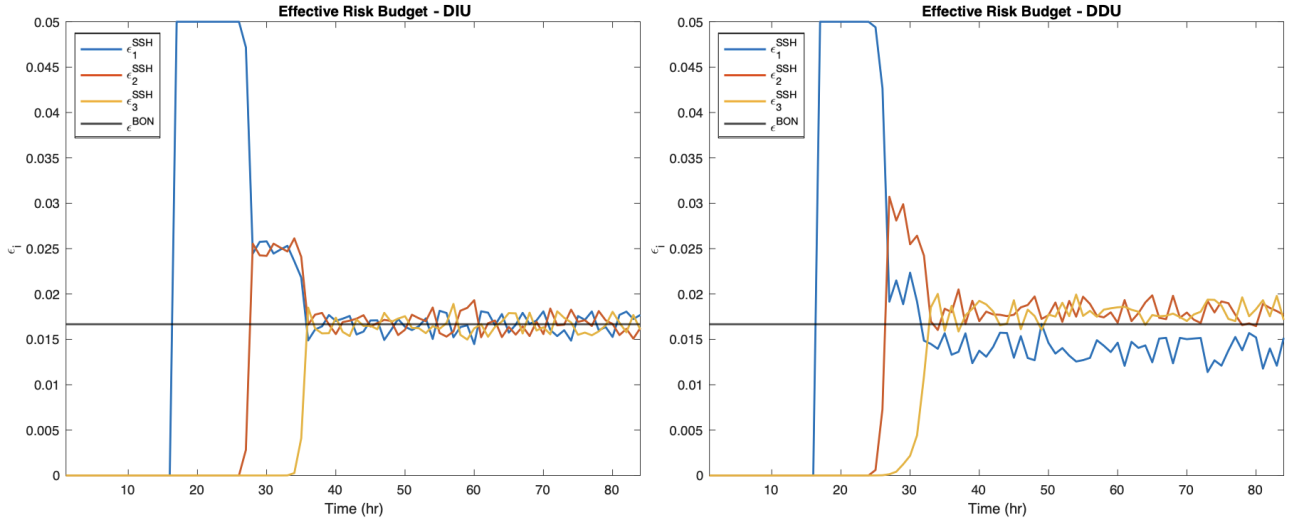

Fig. 7.   Per-unit risk allocation under DET, DIU, and DDU uncertainty frameworks and Bonferroni and SSH solution algorithms.

TABLE II
MONTE CARLO METRICS FOR DROUGHT SCENARIOS

Metric	Algorithm	Uncertainty	System	Unit 1	Unit 2	Unit 3
		DET	2.14	0.013	0.025	0.026
	Bonferroni	DIU	1.79	0.009	0.021	0.023
IVI		DDU	1.51	0.009	0.017	0.019
		DET	2.14	0.0134	0.0247	0.0261
	SSH	DIU	1.80	0.0093	0.0215	0.0232
		DDU	1.53	0.0087	0.0175	0.0196

when uncertainty is modeled explicitly. The same pattern holds under SSH, with DDU again achieving the lowest IVI (1.53). While SSH yields slightly higher system-level IVI under DET and DIU relative to Bonferroni, it maintains comparable or improved performance under DDU. Overall, incorporating decision-dependent uncertainty provides the most significant reliability gains across both algorithms.

C. Flood Scenarios

During the wet season, hydropower operators face the challenge of minimizing spill while maintaining flood margins and generation. Unexpected floods can severely stress the system, leading to potential overtopping above the spill capacity causing flood damage

to surrounding areas. This requires robust reliability measures to ensure the hydropower unit can maintain operations if inflow becomes unexpectedly large. We mimic wet season conditions by initializing all units to start with the initial volume condition of 80% capacity.

Step 1: Learning Wet Season Optimal Trajectories
We present a flood scenario in Fig. 8 under the following settings. Consider an initial estimation of the nominal streamflow to be $q_0 = 0.0475$, which is 5% below the maximum water release bound. The drought event is modeled as two pulses events that occur at 30% and 50% of the simulation period. Each pulse is scaled to have an amplitude of 65% and 85% above the nominal flow each with a length of 8 hours respectively. Each hydropower unit experiences two flood events event that are 12 hours apart, and the flood propagates between units over 18 hours.

Fig. 9 compares the optimal policy trajectories for the cascaded hydropower units under wet season conditions across uncertainty formulations (DET, DIU, DDU) and solution methods (Bonferroni, SSH). Because there is a surplus of inflow and robust initial conditions, all units are able to maintain maximum generation release throughout the duration of the simulation. Therefore, the decision variable with the most degrees of freedom is spill. Because DDU is
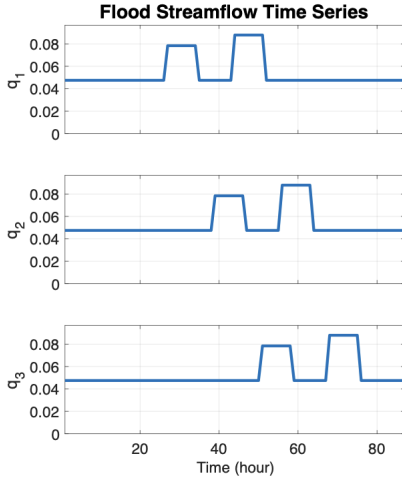
Fig. 8. Time-flow series representing drought scenarios propagating down three cascaded hydropower units in series.

TABLE III

BENCHMARKING ENERGY GENERATION, SPILL, AND EFFICIENCY UNDER FLOOD SCENARIOS

Algorithm	System	DET	DIU	DDU
	System Total [MWh]	58.68	58.66	58.29
	Unit 1	19.78	19.76	19.76
	Unit 2	19.61	19.60	19.36
	Unit 3	19.30	19.30	19.17
Bonferroni	System Spill [m³]	0.88	0.91	1.04
	Unit 1	0.33	0.33	0.33
	Unit 2	0.29	0.30	0.37
	Unit 3	0.26	0.27	0.34
	System Efficiency [MWh/m³]	4.77	4.77	4.74
	System Total [MWh]	58.68	58.66	58.38
	Unit 1	19.78	19.76	19.76
	Unit 2	19.61	19.60	19.42
	Unit 3	19.30	19.30	19.19
SSH	System Spill [m³]	0.88	0.90	1.00
	Unit 1	0.33	0.33	0.33
	Unit 2	0.29	0.30	0.35
	Unit 3	0.26	0.27	0.32
	System Efficiency [MWh/m³]	4.77	4.77	4.75

trained to behave conservatively, we see under that framework the system is encouraged to spill more. This allows the system trained under DDU to maintain more headroom and ends at a lower volume at the terminal state, encoding the value of conservative planning in real-time decision making.

Table III demonstrates that under flood conditions, total system generation converges to the maximum potential across both uncertainty frameworks and solution algorithms. This is a reflection of how the physical constraints (inflow magnitude, generation release bounds) dominate the potential for generation when inflow is in surplus. The DDU framework results in more conservative storage positioning, which increases the likelihood of spill during high inflow realizations but maintains larger flood buffers. We note how the benchmarking table demonstrates how the policies converge under SSH and Bonferroni to the same optimal solution.

Fig. 10 shows the effective risk budgetts that reflect the structural difference between DIU and DDU when subjected to the staggered flood pulses shown in the simulated streamflow series. Under DIU, risk spikes occur only when individual units are subject to the inflow pulses. Under DDU, the system covariance responds to the upstream flood events, creating overlapping risk allocations. Therefore, while the flood hydrograph introduces the same physical pulses in both

TABLE IV

MONTE CARLO METRICS FOR FLOOD SCENARIOS

Metric	Algorithm	System	DET	DIU	DDU
IVI	Bonferroni	System Total	0.0451	0.0404	0.0299
		Unit 1	0.0159	0.0142	0.0142
		Unit 2	0.0153	0.0136	0.0082
		Unit 3	0.0139	0.0126	0.0075
	SSH	System Total	0.0451	0.0413	0.0326
		Unit 1	0.0159	0.0145	0.0144
		Unit 2	0.0153	0.0139	0.0094
		Unit 3	0.0139	0.0129	0.0088
AFV	Bonferroni	System Total [m³]	14.9748	15.7832	19.2775
		Unit 1	3.0734	3.4649	3.4649
		Unit 2	4.6771	4.9676	7.1494
		Unit 3	7.2243	7.3507	8.6632
	SSH	System Total [m³]	14.9748	15.6108	18.2668
		Unit 1	3.0734	3.3771	3.3865
		Unit 2	4.6771	4.9117	6.5867
		Unit 3	7.2243	7.3220	8.2936

cases, DDU internalizes their variance amplification across units, whereas DIU reacts only to exogenous constraint pressure.

Step 2: Real-Time Simulations under Historical Inflow

Using the optimal turbine release and spill policy $u_{i,t}^{(m)*}$ and $s_{i,t}^{(m)*}$ obtained from Stage 1 under uncertainty framework m, we simulate the real-time reservoir volume trajectory under historical streamflow data. Storage then evolves according to

$$V_{i,t}^{(k)} = V_{i,t-1}^{(k)} + q_{i,t}^{hist} - u_{i,t}^{(m)*} - s_{i,t}^{(m)*}. \qquad (21)$$

To quantify preserved flood margin, we define the time-integrated available storage capacity (AFV) as

$$\text{AFV}_i = \frac{1}{K} \sum_{k=1}^{K} \sum_{t=1}^{T} \left(V_i^{\max} - V_{i,t}^{(k)} \right). \qquad (22)$$

The system-level AFV is

$$\text{AFV}_{\text{sys}} = \sum_{i=1}^{n} \text{AFV}_i. \qquad (23)$$

Higher AFV indicates that the policy maintains greater available storage headroom throughout the flood horizon, thereby preserving additional buffering capacity against unexpected inflow shocks.

Table IV shows that under policy testing frameworks, both Bonferroni and SSH exhibit similar structural trends across uncertainty frameworks. As the model shifts from DET to DIU and then to DDU, the Integrated Violation Index (IVI) decreases while the Average Flood Volume (AFV) increases, indicating that more conservative, variance-aware uncertainty frameworks reduces violation severity. SSH achieves slightly lower violation levels under DIU and DDU while maintaining comparable AFV. Overall, the results suggest that uncertainty representation drives the primary behavioral shift, while the solution algorithm refines, but does not fundamentally change, the system's response.also

VI. CONCLUSION

The strategic conservation under DDU leads to higher storage levels and therefore higher hydraulic head later in the horizon, enabling the system to produce more power from the same release volume. In effect, the DDU policy's short-term water savings translate directly into greater long-term value, making it the most revenue-efficient strategy when its uncertainty assumptions align with the true inflow dynamics.

Future work will investigate how the derived risk allocation signals from the supporting hyperplanes algorithm can be used to restore
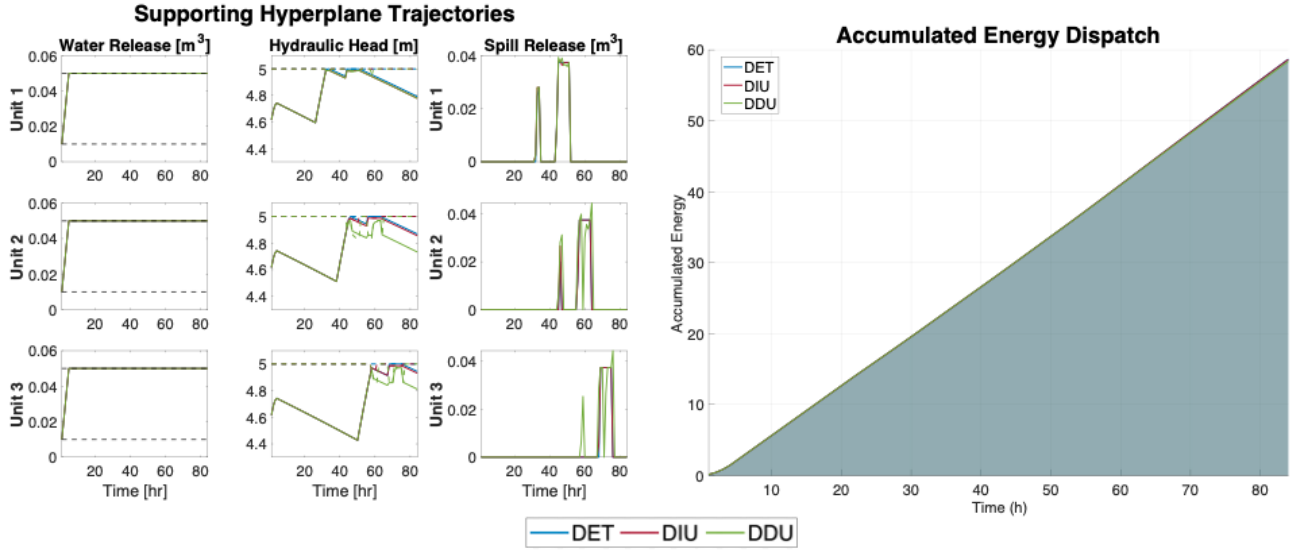
Fig. 9.   Optimal policy trajectories for water release, reservoir volume, and energy generation under DET, DIU, and DDU uncertainty frameworks using the supporting hyperplane solution algorithm during the wet season. Dashed lines indicate operating bounds.
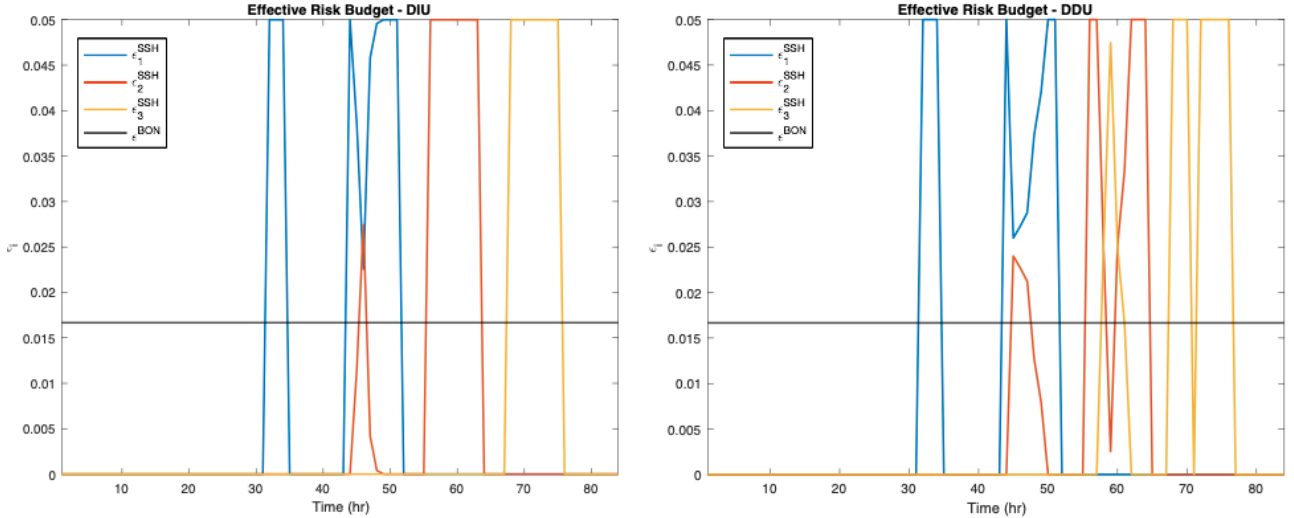

Fig. 10.   Per-unit risk allocation under DET, DIU, and DDU uncertainty frameworks and Bonferroni and SSH solution algorithms.

reservoir operations to a safe level under extreme droughts and floods. Furthermore, adding in a mechanism to quantify the value of storage will solidify the methods here in the medium-term planning framework. It's important to balance immediate benefit versus future benefit, especially when straddling multiple time horizons.

APPENDIX

For the following proofs, the simplified notation set is used

$$\varphi_t(x_t) = \mathbb{P}[a + Ax_t \leq \xi_t \leq b + Ax_t]$$
$$= F_{\xi_t}[\underline{V}(x_t), \tilde{V}(x_t)] \quad (24a)$$

$$A = L_T \quad (24b)$$
$$a = \underline{V} - \mathbb{1}V_0 - L_T Q \quad (24c)$$
$$b = \overline{V} - \mathbb{1}V_0 - L_T Q \quad (24d)$$

Where L_T is the lower triangular unit matrix, V are the volume vectors and Q is the inflow vector without the process uncertainty.

First, we show that any feasible solution to (10) is also feasible for (1).

Lemma 2: *Feasibility:* Assume that $p > 0.5$ and that $\xi \in \mathbb{R}^m$ is a symmetric random variable. Then the feasible set of (10) is contained in the feasible set of (1).

Proof: Assume that $x \in \mathcal{R}^n$ is not feasible for (1). Using the matrix notation derived in (10), we observe that (1) can leverage the same matrix notation with $\xi = 0$, decomposing the chance constraint into two inequality constraints.

Without loss of generality, we assume the violated constraint is $Ax \leq a$ and that the first component of x is strictly positive. Then

$$\mathbb{P}[a + Ax \leq \xi \leq b + Ax] \leq \mathbb{P}[a + Ax \leq \xi]$$
$$\leq \mathbb{P}[e_1^T(a + Ax) \leq e_1^T \xi] \leq \mathbb{P}[0 \leq \xi] < 0.5 \quad (25)$$

In Step 1, we use the symmetrical property of ξ and remove the upper bound. In Step 2, we isolate the positive entry of x using e_1^T, the standard unit vector of $\mathbb{R}^m$. Step 3 uses the initial assumption that $e_1^T(a + Ax) \geq 0$, and Step 4 uses the zero-mean symmetrical

property of ξ to complete the proof, showing that x can't be feasible for (10).

Theorem 2: *Convergence under Finite Iterations:* If the Sequential Supporting Hyperplane (SSH) algorithm terminates in K iterations, then it has converged to the optimal solution of the L-JCCP under DDU with tolerance ε_{LP}.

Proof: First note that the function $\varphi_t(x)$ is logarithmically concave under Gaussian distributions and its feasible set $\Omega_t = \{x_t : \varphi_t(x_t) \geq p\}$ is convex. This is an established property from Prekopa in [5]. Using this property, we can establish the monotonic refinement relationship. Namely

$$\Omega_t \subseteq \mathcal{P}_t^K \subseteq ... \subseteq \mathcal{P}_t^1 \subseteq \mathcal{P}_t^0 \tag{26}$$

where $\mathcal{P}_t^k = \{x_t \geq 0 : A_t^k x_t \leq b_t^k\}$ is the feasible region generated by solving the LP at iteration k and time t. We establish this result by noting the result x_t^k obtained from solving the LP implies that $\varphi_t(x_t^k) < p$ and $x_t^k \notin \Omega_t$. Since $\varphi_t(\cdot)$ is continuous, the intermediate value theorem guarantees the existence of $\lambda^* \in (0, 1]$ that finds x_t^{k*} such that $\varphi_t(x_t^{k*}) = p$ with tolerance ε_R.

Because $\varphi_t(\cdot)$ is concave at x_t^{k*}, the supporting hyperplane generated at iteration k and time t establishes the following

$$p \leq \varphi_t(x_t) \leq \varphi_t(x_t^{k*}) + \nabla\varphi_t(x_t^{k*})^T(x_t - x_t^{k*}) \tag{27a}$$

$$p \leq \varphi_t(x_t) \leq p + \nabla\varphi(x_t^{k*})^T(x_t - x_t^{k*}) \tag{27b}$$

$$0 \leq \nabla\varphi_t(x_t^{k*})^T(x_t - x_t^{k*}) \tag{27c}$$

$$-\nabla\varphi_t(x_t^{k*})^T x_t \leq -\nabla\varphi_t(x_t^{k*})^T x_t^{k*} \tag{27d}$$

As a corollary, the hyperplane constraint separates x_t^k from the estimated feasible region and establishes monotonic refinement.

When the SSH algorithm terminates after K iterations, x_t^{K+1} is optimal the solution to the LP defined by $\mathcal{P}_t^K$. By the upper boundary of stopping criteria, we establish that

$$\frac{c^T(x_t^{K*} - x_t^{K+1})}{c^T x_t^{K+1}} = \varepsilon_{LP} \tag{28a}$$

$$x_t^{K*} = (1 + \varepsilon_{LP})x_t^{K+1} \tag{28b}$$

Therefore, x_t^{K*} gives the optimal value to the objective function of the L-JCCP with tolerance ε_{LP} in the feasible region of $\mathcal{P}_t^K$. From Eq. (26), we know that $\mathcal{P}_t^K$ includes the feasible set Ω_t. Since x_t^{K*} satisfies the joint chance constraint $\varphi(x_t^{K*}) \geq p$, it is also in the feasible region Ω_t. Because x_t^{K*} minimizes the objective function within $\mathcal{P}_t^K$ and $x_t^{K*} \in \Omega_t$, x_t^{K*} is also an optimal solution to the L-JCCP at time t.

Finally, we concatenate all of the optimal decisions x_t^* for $t = [1, ..., T]$ to form the optimal decision vector x^* over the entire horizon.

Theorem 3: *Convergence under Infinite Iterations:* The SSH algorithm either finds a global optimizer to the L-JCCP in a finite number of iterations or it generates a sequence $\{x_t^{k_i}\}_{i=1}^\infty$ converging to the global optimizer.

Proof: We first show that the sequence will generate at least one convergent subsequence $\{x_t^{k_i}\}_{i=1}^\infty$ if it does not converge in a finite number of iterations. We remark that sets $\{\mathcal{P}_t^0, \mathcal{P}_t^1, ...\}$ are compact because they are generated from a series of intersecting half-spaces and the original feasible region from (1), which is a closed and bounded subset of Euclidean space. Therefore, $\{x_t^{k_i}\}_{i=1}^\infty$ is a bounded sequence of real numbers and it has a convergent subsequence by the Bolzano-Weierstrass theorem.

Next, we show that the limit point of a convergence subsequence $\{x_t^{k_i}\}_{i=1}^\infty$ is a global minimum of L-JCCP. Because each set $\mathcal{P}_t^k$ overestimates Ω_t, $c^T x_t^{k_i}$ gives a lower bound on the optimal value of the objective function. From the monotonic refinement relation and its corollary on separating hyperplanes, we know that $\{c^T x_t^{k_i}\}_{i=1}^\infty$ is non-decreasing. We can also conclude that $\lim_{i\to\infty} c^T x_t^{k_i} = c^T \tilde{x}_t$, where $\tilde{x}_t \in \Omega_t$ is the limit point of the sequence. Therefore, the SSH algorithm will generate a sequence converging to the global optimum of the L-JCCP.

REFERENCES

[1] B. Tong, Q. Zhai, and X. Guan, "An MILP based formulation for short-term hydro generation scheduling with analysis of the linearization effects on solution feasibility," *IEEE Trans. Power Syst.*, vol. 28, no. 4, pp. 3588–3599, Nov. 2013.

[2] T. M. Souza, "An accurate representation of water delay times for cascaded reservoirs in hydro scheduling problems," in *2012 IEEE Power and Energy Society General Meeting.* IEEE, Jul. 2012, pp. 1–7.

[3] N. Qi, N. Zheng, and B. Xu, "Chance-constrained energy storage pricing for social welfare maximization," *arXiv [eess.SY]*, Jul. 2024.

[4] A. Hamann, G. Hug, and S. Rosinski, "Real-time optimization of the mid-columbia hydropower system," *IEEE Trans. Power Syst.*, vol. 32, no. 1, pp. 157–165, Jan. 2017.

[5] A. Prékopa and T. Szántai, "Flood control reservoir system design using stochastic programming," in *Mathematical Programming in Use.* Berlin, Heidelberg: Springer Berlin Heidelberg, 1978, pp. 138–151.

[6] T. Szantai, "A computer code for solution of probabilistic-constrained stochastic programming problems," in *Springer Series in Computational Mathematics*, ser. Springer series in computational mathematics. Berlin, Heidelberg: Springer Berlin Heidelberg, 1988, pp. 229–235.

[7] C. Ordoudis, V. A. Nguyen, D. Kuhn, and P. Pinson, "Energy and reserve dispatch with distributionally robust joint chance constraints," *Oper. Res. Lett.*, vol. 49, no. 3, pp. 291–299, May 2021.

[8] W. van Ackooij, R. Henrion, A. Möller, and R. Zorgati, "Joint chance constrained programming for hydro reservoir management," *Optim. Eng.*, vol. 15, no. 2, pp. 509–531, Oct. 2013.

[9] J.-C. Alais, P. Carpentier, and M. De Lara, "Multi-usage hydropower single dam management: chance-constrained optimization and stochastic viability," *Energy Syst.*, vol. 8, no. 1, pp. 7–30, Feb. 2017.

[10] S. W. D. Turner, J. C. Steyaert, L. Condon, and N. Voisin, "Water storage and release policies for all large reservoirs of conterminous united states," *J. Hydrol. (Amst.)*, vol. 603, no. 126843, p. 126843, Dec. 2021.

[11] E. Cohn, N. Qi, U. Lall, and B. Xu, "A lagrangian-informed long-term dispatch policy for coupled hydropower and photovoltaic systems," in *2025 IEEE Power & Energy Society General Meeting (PESGM).* IEEE, Jul. 2025, pp. 1–5.

[12] H. Zhang, K. Liao, J. Yang, Z. Yin, and Z. He, "Long-term and short-term coordinated scheduling for wind-PV-hydro-storage hybrid energy system based on deep reinforcement learning," *IEEE Trans. Sustain. Energy*, vol. PP, no. 99, pp. 1–13, 2025.

[13] W. Yuan, S. Zhang, C. Su, Y. Wu, D. Yan, and Z. Wu, "Optimal scheduling of cascade hydropower plants in a portfolio electricity market considering the dynamic water delay," *Energy (Oxf.)*, vol. 252, no. 124025, p. 124025, Aug. 2022.

[14] J. Kong, H. I. Skjelbred, and O. B. Fosso, "An overview on formulations and optimization methods for the unit-based short-term hydro scheduling problem," *Electric Power Syst. Res.*, vol. 178, no. 106027, p. 106027, Jan. 2020.

[15] B. A. Faber and J. R. Stedinger, "Reservoir optimization using sampling SDP with ensemble streamflow prediction (ESP) forecasts," *J. Hydrol. (Amst.)*, vol. 249, no. 1-4, pp. 113–133, Aug. 2001.

[16] J. D. Hamilton, *Time series analysis.* Princeton, NJ: Princeton University Press, 1994.

[17] T. Bollerslev, "Modelling the coherence in short-run nominal exchange rates: A multivariate generalized arch model," *Rev. Econ. Stat.*, vol. 72, no. 3, p. 498, Aug. 1990.

[18] A. Meister and J.-P. Kreiß, "Statistical inference for nonparametric GARCH models," *Stoch. Process. Their Appl.*, vol. 126, no. 10, pp. 3009–3040, Oct. 2016.

[19] A. Genz, "Numerical computation of multivariate normal probabilities," *J. Comput. Graph. Stat.*, vol. 1, no. 2, pp. 141–149, Jun. 1992.

[20] W. Van Ackooij, R. Henrion, A. Möller, and R. Zorgati, "On probabilistic constraints induced by rectangular sets and multivariate normal distributions," *Math. Methods Oper. Res. (Heidelb.)*, vol. 71, no. 3, pp. 535–549, Jun. 2010.

[21] J. Kronqvist, A. Lundell, and T. Westerlund, "The extended supporting hyperplane algorithm for convex mixed-integer nonlinear programming," *J. Glob. Optim.*, vol. 64, no. 2, pp. 249–272, Feb. 2016.